ACS APPLIED MATERIALS & INTERFACES

Research Article

www.acsami.org

A Molecular Tetrapod for Organic Photovoltaics

Jianzhong Yang, Zhen Zhang, and Yang Qin*

Department of Chemistry & Chemical Biology, University of New Mexico, MSC03 2060, 1 UNM, Albuquerque, New Mexico 87131, United States

Supporting Information

ABSTRACT: The synthesis and characterization of a molecular tetrapod, **SFBTD**, featuring a tetraphenylsilane center and four identical conjugated arms, which structurally resembles breakwaters in common wave-reducing shore constructions, are reported. Cyclic voltammetry reveals that **SFBTD** has a medium band gap of ca. 2.0 eV and a low-lying HOMO energy level at ca. −5.2 eV. Absorption spectroscopy, X-ray diffraction, and differential scanning calorimetry experiments reveal a low degree of crystallinity in this compound and slow crystallization kinetics. Bulk heterojunction organic photovoltaics (OPVs) employing **SFBTD** and fullerene derivatives exhibit power conversion efficiencies (PCEs) up to 1.05% and open-circuit voltage (V_{OC}) values as high as 1.02 V. To the best of our knowledge, this is the highest PCE obtained for OPVs employing molecular tetrapods as donor materials. These devices are relatively thermally stable due to the known ability of breakwater tetrapods to interlock, preventing dislodging and sliding. The lack of favorable phase separations and low hole mobilities of the blend films are the major factors limiting the device performance. Ternary blend devices by the addition of three low band gap poly(thienylene vinylene) (PTV) derivatives were fabricated and tested. We found that the added PTVs acted to be either the major hole conductor or a competing hole conduction channel depending on the HOMO level positions relative to that of **SFBTD**. Some of the ternary OPV devices outperformed the corresponding binary counterparts employing **SFBTD** or PTVs alone, suggesting cooperative effects in the ternary systems.

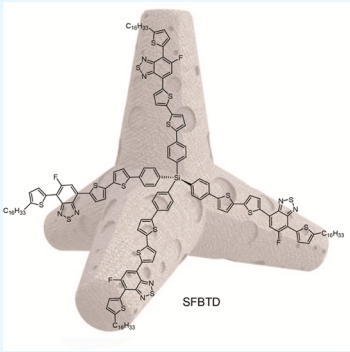

KEYWORDS: *tetrapod, small molecule, organic photovoltaic, ternary blend, morphology*

INTRODUCTION

Among various types of alternative renewable energy sources, organic photovoltaics (OPVs) are considered as a promising low-cost candidate.[1] Current research in OPVs has been dominated by conjugated polymers (CPs) due to the versatility in structure−property variations, thin film forming ability, and amenability to low-cost, large throughput fabrication techniques.[2−4] Bulk heterojunction (BHJ) polymer solar cells (PSCs) with power conversion efficiencies (PCEs) over 10% have now been achieved in recent years.[5−12] However, the cross-coupling reactions employed in CP syntheses are typically step-growth polymerization techniques that result in large distribution of molecular weights and frequently in structural defects. Besides, variations are common in CP synthesis from different batches and even different laboratories, which further limit mass production and device improvement.

In recent years, many conjugated small molecules have been applied in OSCs. Compared with their polymeric counterparts, small molecules are more repeatable in synthesis and offer unique fabrication methods such as vacuum deposition. Furthermore, the crystalline nature of conjugated small molecules often leads to high charge conductivities.[13−21] Such attributes have drawn significant investigation and sustainable efforts toward the development of conjugated small molecules BHJ OSC devices, the PCEs of which have been steadily improved to rival those of PSCs.[22−29]

Current research on small molecule OPVs has been mainly focused on conjugated chromophores having linear structures containing multiple aromatic moieties in series. Charge transport through such one-dimensional (1-D) structures is expected to be anisotropic and very sensitive to molecular packing and crystallinity of the molecules. Furthermore, the high crystalline nature of linear molecules often leads to uneven thin films possessing large grain boundaries, which unfavorably impact device performances. Small molecules possessing three-dimensional (3-D) geometries, on the other hand, have received relatively little attention.[21] Due to the isotropic and symmetrical structures, increased absorption cross sections and more extensive percolating pathways for charge transport in these molecules are expected. Among 3-D molecules, molecular tetrapods are especially intriguing since these breakwater-like structures are able to mutually interlock to prevent dislodging, potentially leading to improved device stability.[30−32]

Received: May 27, 2016
Accepted: August 12, 2016
Published: August 12, 2016

DOI: 10.1021/acsami.6b06365
ACS Appl. Mater. Interfaces 2016, 8, 22392−22401

Examples of molecular tetrapods in OPV applications have been scarce. In 2006, Roncali and co-workers reported the first two examples of molecular tetrapods applied in OPVs.[33] These tetrapods contain a silicon center and four terthiophene arms end-capped, respectively, with alkyl and thioalkyl moieties arranged in space in tetrahedral fashion. The OPV performances of these tetrapods were relatively poor, which the authors ascribed to the large band gaps of these molecules. Köse and co-workers also synthesized a medium band gap molecular tetrapod by attaching four linear push−pull type chromophores containing benzothiadiazole (BTD) units to a silicon center.[34] They found larger charge mobilities in these tetrapods over those of their linear analogues in disordered media, which they attributed to the high dimensionality of tetrapods. We have recently reported a stable breakwater-like tetrapod **SO** (Scheme 1) composed of a silane center and four arms containing a phenyl ring and a terthiophene group functionalized with cyanoester side chains.[35] We found that **SO** was extremely difficult to crystallize and no phase separations could be observed in blend films of **SO** with the common electron acceptor $PC_{61}BM$ ([6,6]-phenyl-C_{61}-butyric acid methyl ester).[35] Surprisingly, we also found that the linear model compound **MO** (Scheme 1) possessed similarly slow crystallization kinetics, from which we speculated that the structure of each of the **SO** arms is the intrinsic reason that causes the slow crystallization behavior. Nevertheless, among all the above examples, the 3-D tetrapodal donor materials always out-performed the corresponding 1-D linear π-conjugated arms, which mainly resulted from the isotropic optical and charge-transporting properties associated with the 3-D geometry.

Scheme 1. Structures of SO and MO

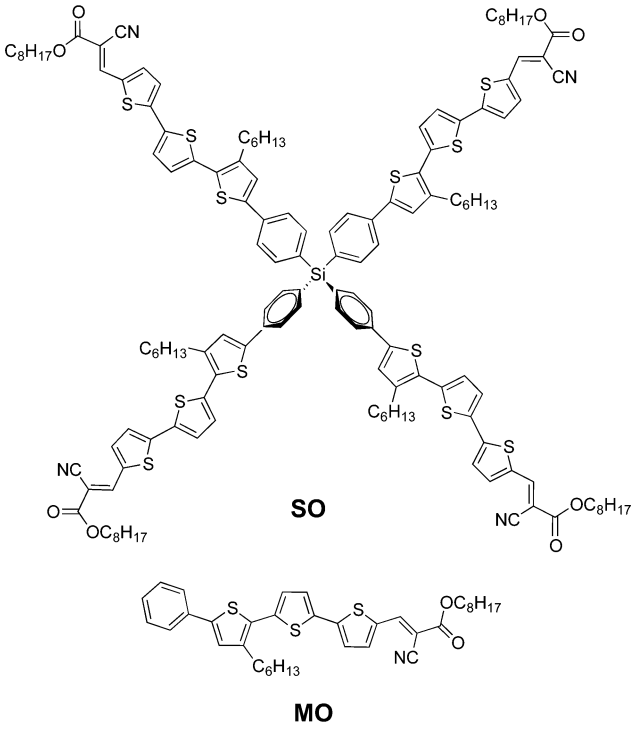

Since our previous studies on **SO** and **MO** indicate that the slow crystallization behavior in the tetrapod may intrinsically originate from each of its arms, we conjecture that we may be able to increase the crystallization kinetics of these tetrapods by removing the alkyl side chains in the middle of each arm and by using more rigid and planar electron-accepting moieties such as the fluorinated benzothiadiazole (FBTD) units. Meanwhile, the attachment of fluorine atoms to conjugated frameworks can potentially lead to increased internal dipole moments, which provides extra driving forces to induce phase separations within the blend films.[36−38] Furthermore, the strongly electron-withdrawing effects of fluorine atoms can lower the energies of both the frontier orbitals (HOMO and LUMO) without significantly affecting the band gaps of conjugated molecules.[39] Therefore, increased open-circuit voltage (V_{OC}) values are expected due to the deepened HOMO levels without changing the desired light-harvesting properties.[40] We report herein a stable molecular tetrapod, **SFBTD**, containing a tetraphenylsilane center and four arms composed of one FBTD and three thiophene units. **SFBTD** shows excellent thermal stability and solution processability, strong absorption in a broad spectral range, and frontier energy levels matching those of fullerene acceptors. BHJ OPVs based on **SFBTD**/$PC_{61}BM$ without any additives and interfacial engineering exhibit PCEs as high as 1.05% with high V_{OC} values up to 1.02 V. To the best of our knowledge, this is the highest PCE reported for OPV devices using molecular tetrapods as donor materials.

RESULTS AND DISCUSSION

Synthesis and Characterization. Synthetic details for the molecular tetrapod **SFBTD**, and the linear model compound **MFBTD**, are summarized in Scheme 2 and included in the Supporting Information (SI). Compound **9** was synthesized according to previously reported procedures.[35] Compound **10** was prepared from **9** through Suzuki coupling reactions with bis(pinacolato)diboron. Compounds **9** and **10** can conveniently serve as common cores for constructing different 3-D molecular tetrapods by grafting with different arms. After Suzuki coupling reactions of **10** with 4 equiv of **8**, **SFBTD** was obtained by column chromatography and shows excellent solubility in common processing solvents such as $CHCl_3$, tetrahydrofuran (THF), and nonpolar aromatic solvents. The 2-hexyldecyl side chains on **SFBTD** are necessary to ensure solubility of the tetrapod, since initial attempts at preparing **SFBTD** analogues without alkyl side chains and with linear alkyl side chains all failed due to precipitation of reaction intermediates. ^1H and ^{13}C NMR spectroscopy were employed to characterize the newly prepared compounds, which match well with expected structures (SI). The tetrapodal structure of **SFBTD** was confirmed by high-resolution mass spectrometry (HR-MS), giving a measured molar mass of 2825.7766 [M^+] that matches reasonably well with the calculated value of 2824.9255 [M^+]. The slightly larger than expected discrepancy is presumably caused by the significantly lower molar mass of the calibration standard applied (cholesterol, m/z = ca. 369). In order to supplement the HR-MS experiments, we have also performed elemental analysis on **SFBTD**, giving measured elemental contents of C, H, N at 67.95, 6.54, and 3.75%, matching well with the calculated values at 67.95, 6.27, and 3.96%, respectively.

We employed UV−vis absorption and fluorescence spectroscopies to investigate the electronic properties of **SFBTD** and **MFBTD** in both dilute solutions and as thin films (Figure 1). Chlorobenzene solutions (10^{-5} M) of **SFBTD** and **MFBTD** exhibit almost identical absorption profiles that are structureless with two major transition peaks at ca. 504 and 384 nm, and indistinguishable fluorescence spectra with λ_{em}'s at ca. 620 nm.

DOI: 10.1021/acsami.6b06365
ACS Appl. Mater. Interfaces 2016, 8, 22392−22401

Scheme 2. Synthesis of SFBTD and MFBTD

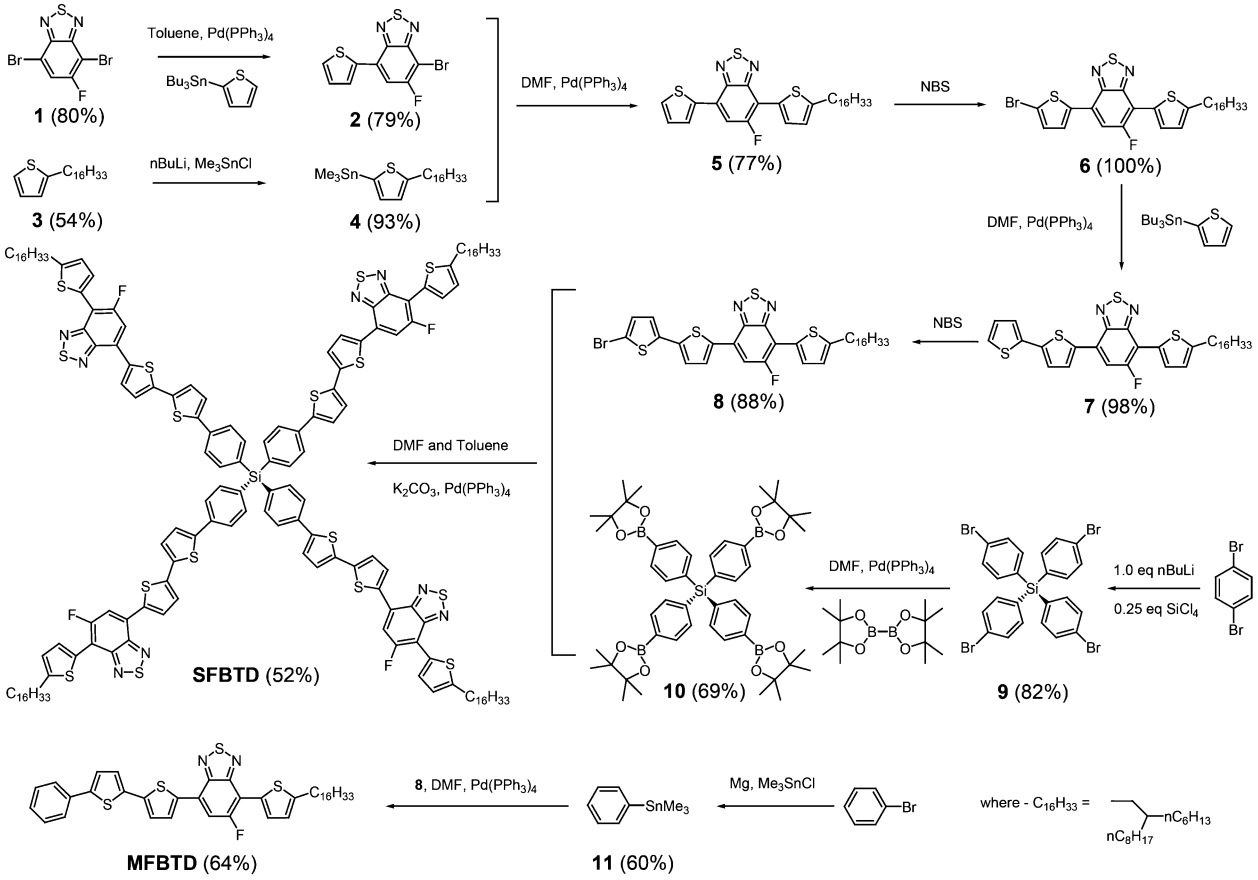

The emission quantum efficiencies of **SFBTD** and **MFBTD** are calculated to be also similar, at ca. 3.4% and ca. 4.1%, respectively. The similarity in solution optical properties between **SFBTD** and **MFBTD** suggests that the four conjugated arms of **SFBTD** have negligible electronic communications. We assign the electronic transition at 504 nm to intramolecular charge transfer (ICT) transition and the other at 384 nm to largely $\pi-\pi^*$ transition mixed with certain degrees of ICT character. We base these assignments on time-dependent density functional theory (TD-DFT) calculations as shown in Figure S1. The geometry optimization was performed on **MFBTD**, with a methyl group replacing the long alkyl side chain, applying the B3LYP functional with the 6-31G* basis set in Gaussian 09.[41] TD-DFT was performed on the optimized geometry only using the same functional and basis set. Two bright singlet states, namely, S1 and S3, having transition energies at 2.07 and 3.02 eV, which correspond to transitions from HOMO to LUMO and HOMO to LUMO+1 orbitals, respectively, are found. The S1 state clearly has charge transfer characteristics with hole density delocalized throughout the entire chromophore, while the electron density is mainly localized at the electron-poor FBTD unit. The S3 state, on the other hand, possess largely $\pi-\pi^*$ character with large overlap between the hole and electron densities. From the simulated absorption spectrum, the S3 state transition energy more closely matches that of the absorption peak at 384 nm (3.02 eV vs 3.22 eV), while the S1 state transition energy is much lower than observed (2.07 eV vs 2.46 eV), since TD-DFT is known to be problematic in estimating energies of charge transfer states.[42]

The extinction coefficient (ε) of **SFBTD** is calculated to be ca. 1.3×10^5 L mol^{-1} cm^{-1} based on concentrations of the molecular tetrapod, corresponding to an $\varepsilon = 3.3 \times 10^4$ L mol^{-1} cm^{-1} for each of its arms. **MFBTD**, on the other hand, displays an $\varepsilon = 2.8 \times 10^4$ L mol^{-1} cm^{-1} in solution. The seemingly stronger absorption observed for **SFBTD**, on per arm basis, is presumably caused by its more isotropic structure and thus larger absorption cross section.[33] As expected from the different molecular geometries, thin films of **SFBTD** and **MFBTD** display largely different electronic properties. Neat thin films of **SFBTD** show a λ_{max} at ca. 525 nm, slightly red-shifted by 25 nm when compared with that of the solution profile. This red shift is likely a solid state phenomenon in which the conjugated chains become slightly more planar due to packing interactions, thus leading to longer conjugation lengths and lower transition energies. When excited at the λ_{max}, **SFBTD** thin films show very weak fluorescence and a λ_{em} at ca. 650 nm, giving a large Stoke's shift of 125 nm. Interestingly, the two major electronic transitions of **MFBTD** are both blue-shifted in thin films. The ICT peak shifts to 457 nm, and a shoulder peak at ca. 550 nm is observed that matches well with the ICT transition of **SFBTD** thin films. We conjecture that **MFBTD** behaves similarly to **SFBTD** in the solid state and, due to its linear shape, **MFBTD** can form H-type aggregates, leading to the observed blue shift in absorption spectra.[43] Emission of **MFBTD** films is thus expectedly quenched to a large extent, and only a weak fluorescence peak can be seen at ca. 660 nm. The optical band gaps of **SFBTD** and **MFBTD** are thus estimated from the absorption edges to be both ca. 2.2 eV in solutions and 2.0 eV in thin films, respectively.

DOI: 10.1021/acsami.6b06365
ACS Appl. Mater. Interfaces 2016, 8, 22392−22401

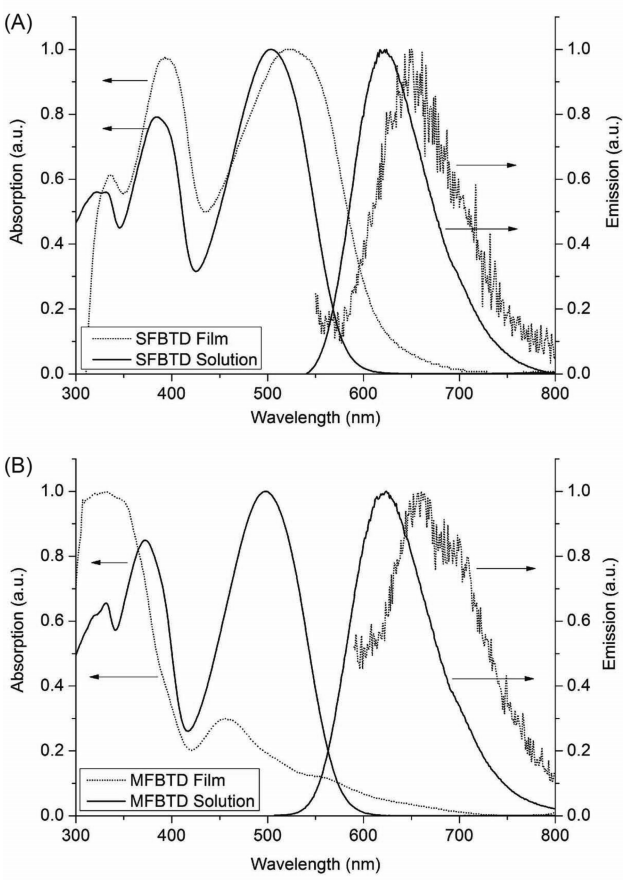

Figure 1. UV−vis absorption (left axis) and emission (right axis) spectra of (A) **SFBTD** and (B) **MFBTD** in chlorobenzene solutions (10^{-5} M, solid lines) and as thin films (dashed lines).

The frontier energy levels and band gaps of **SFBTD** and **MFBTD** in solutions and thin films are estimated through cyclic voltammetry (CV). The recorded voltammograms were referenced externally to ferrocene (Fc) redox couple (−4.80 eV). As depicted in Figure S2, very similar redox behaviors of both **SFBTD** and **MFBTD** are observed in both solutions and thin films. In solutions, two quasi-reversible oxidation waves with onsets at ca. 0.4 and 0.9 V for **SFBTD** and at ca. 0.5 and 0.8 V for **MFBTD** are observed. Two quasi-reversible reduction peaks with onsets at ca. −1.6 and −2.1 V are recorded for both **SFBTD** and **MFBTD**. From onsets of the first oxidation and reduction waves, the HOMO and LUMO levels of **SFBTD** are estimated to be −5.2 and −3.2 eV, while the HOMO and LUMO levels of **MFBTD** are estimated to be −5.3 and −3.2 eV, respectively. Therefore, electrochemical band gaps of 2.0 and 2.1 eV are calculated for **SFBTD** and **MFBTD**, respectively, agreeing reasonably well with UV−vis measurements. In thin films, four irreversible oxidation waves and three quasi-reversible reduction waves are observed for both **SFBTD** and **MFBTD**. The onsets of first oxidation and reduction waves are located at ca. 0.7 and −1.3 V for **SFBTD** and at ca. 0.6 and −1.4 V for **MFBTD**, respectively. The HOMO and LUMO levels of **SFBTD** in the solid state are thus estimated, respectively, at −5.5 and −3.5 eV, while the HOMO and LUMO levels of **MFBTD** are calculated to be −5.4 and −3.4 eV, respectively. Thus, electrochemical band gaps of both **SFBTD** and **MFBTD** thin films are calculated as 2.0 eV, matching well with UV−vis measurements.

We employed differential scanning calorimetry (DSC) measurements to investigate the thermal properties of **SFBTD** and **MFBTD**, and the results are displayed in Figure 2. Unlike the slow crystallization kinetics observed for the

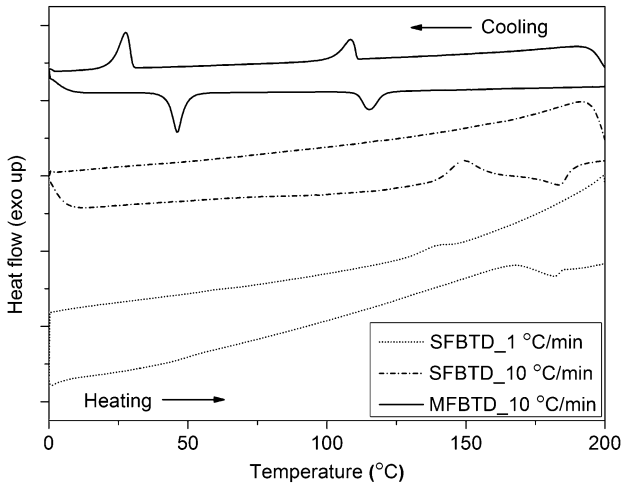

Figure 2. Differential scanning calorimetry (DSC) histograms of **MFBTD** at 10 °C/min (solid line), and of **SFBTD** at scanning rates of 10 °C/min (short dashed-dotted line) and at 1 °C/min (dotted line). Second heating and cooling curves are shown.

similar model compound **MO** we reported previously[35] and for a structurally twisted linear conjugated small molecule reported by Bazan et al.,[44] **MFBTD** shows much enhanced crystallinity. At the typical heating/cooling rate of 10 °C/min, **MFBTD** displays two melting peaks at ca. 46 °C and ca. 115 °C in the heating curve and two crystallization transitions at ca. 28 °C and ca. 108 °C upon cooling. In the case of **SFBTD**, however, we observed an exothermic peak at ca. 150 °C and one melting transition at ca. 183 °C during heating events and no thermal transitions during cooling. On the other hand, when we reduced the heating/cooling rate to 1 °C/min, we observed the crystallization transition only in the cooling curves at ca. 140 °C, suggesting slow crystallization rates of **SFBTD**. As a result, the slow crystallization kinetics of **SFBTD**, as well as that of **SO**, is most likely caused by their 3-D molecular geometry and not intrinsically by the nature of the constituting arms as we previously speculated. We further confirmed such solid-state characteristics of **SFBTD** and **MFBTD** by using X-ray diffraction (XRD) experiments on thin films drop-cast onto glass substrates from chlorobenzene solutions, as shown in Figure S3. No obvious scattering peaks are observed in the thin films of **SFBTD**, whereas, in the thin films of **MFBTD**, we observed two sharp scattering peaks at 2θ values of ca. 2.8° and 3.2°, corresponding to *d*-spacings of ca. 3.2 and 2.8 nm, respectively. This indicates that **MFBTD** exhibits better crystallinity and more ordered solid-state packing than **SFBTD**, as found in our DSC studies.

Binary Blend Devices. We first fabricated BHJ OPV devices by adopting conventional device geometries: ITO/MoO_3 (10 nm)/active layer/Al (100 nm). The active layer was prepared by spin-coating the chloroform blend solution of **SFBTD** or **MFBTD** with $PC_{61}BM$ at predetermined weight ratios. Optimization of OPV devices was thoroughly investigated by changing the thermal annealing temperature, and the best condition was found to be thermal annealing at 80 °C for 15 min. Photovoltaic performances of devices by representative

DOI: 10.1021/acsami.6b06365
ACS Appl. Mater. Interfaces 2016, 8, 22392−22401

Table 1. Summary of Device Performance Data of Organic Solar Cells Employing SFBTD and MFBTD under Various Fabrication Conditions[a]

	ratios[b]	V_{OC} (V)	J_{SC} (mA/cm^2)	FF (%)	PCE (%)
SFBTD/$PC_{61}BM$	2.5/7.5	0.87 ± 0.04 (0.90)	2.84 ± 0.17 (3.09)	30 ± 0.89 (31)	0.74 ± 0.04 (0.81)
	2.5/10.0	0.88 ± 0.03 (0.92)	3.64 ± 0.17 (3.86)	33 ± 1.83 (35)	1.05 ± 0.06 (1.11)
	2.5/12.5	0.85 ± 0.01 (0.86)	2.46 ± 0.11 (2.62)	31 ± 0.42 (32)	0.66 ± 0.02 (0.69)
MFBTD/$PC_{61}BM$	2.5/2.5	0.74 ± 0.02 (0.77)	1.15 ± 0.13 (1.41)	27 ± 0.97 (28)	0.23 ± 0.02 (0.28)
	2.5/5.0	0.85 ± 0.01 (0.86)	2.41 ± 0.10 (2.61)	27 ± 0.35 (27)	0.55 ± 0.03 (0.58)
	2.5/7.5	0.79 ± 0.02 (0.81)	1.17 ± 0.15 (1.29)	28 ± 0.56 (28)	0.25 ± 0.03 (0.28)

[a]Thermal annealing at 80 °C for 15 min. Averages of five individual cells are reported; the highest values are given in parentheses. [b]All ratios by weight.

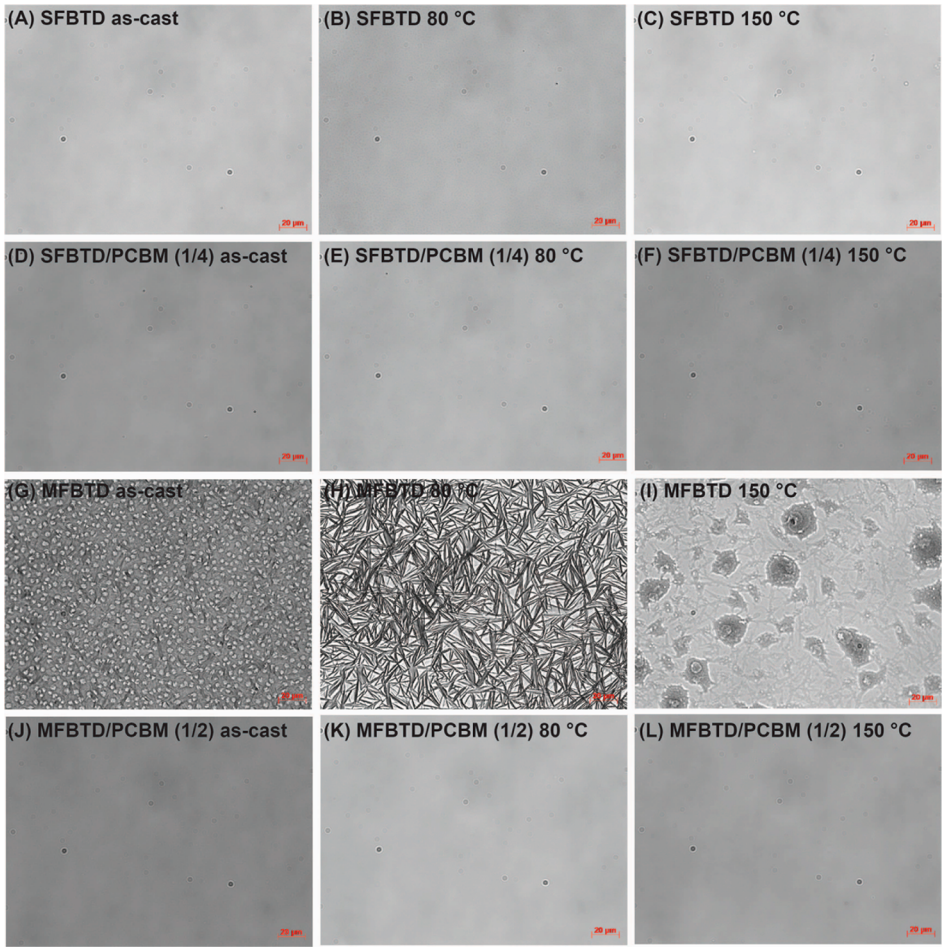

Figure 3. Optical micrographs (400× magnification) of thin films of **SFBTD** (A–C), **MFBTD** (G–I), and corresponding $PC_{61}BM$ blend films (D–F and J–L) under different thermal annealing conditions. Scale bars in all: 20 μm.

fabrication conditions are summarized in Table 1, and the optimized devices' current density–voltage (I–V) curves are depicted in Figure S4. Under optimized fabrication conditions, devices from **SFBTD** consistently out-perform those using **MFBTD**. **SFBTD** and **MFBTD** devices gave open-circuit voltage (V_{OC}) values up to 0.88 and 0.85 V, respectively, which are relatively high values among OPVs. Meanwhile, V_{OC}'s of both **SFBTD** and **MFBTD** devices are relatively insensitive to the donor/acceptor weight ratios. Devices employing **SFBTD**/$PC_{61}BM$ at a weight ratio of 1/4 and **MFBTD**/$PC_{61}BM$ at a weight ratio of 1/2 give the best performance. The best **SFBTD** device has a short-circuit current (J_{SC}) of 3.64 mA/cm^2, a fill factor (FF) of 33%, and the PCE of ca. 1.05%. The best **MFBTD** devices display a J_{SC} of 2.41 mA/cm^2 and a FF of 27%, leading to a PCE of ca. 0.55%. Both **SFBTD** and **MFBTD** devices suffer greatly from low J_{SC} and FF values. We believe that significant charge recombination is responsible for the low current and FF values, as suggested by the large current increase at negative bias under light in both devices. We also observed similar behaviors for our previous molecular tetrapod **MO**, for which we found that inferior blend morphologies and low charge mobilities were mainly responsible for the low device performances.[35] We thus employed optical microscopy to study the morphologies of neat films of **SFBTD** and **MFBTD** as well as those of the corresponding $PC_{61}BM$ blend films, and the micrographs are included in Figure 3.

SFBTD thin films either as-cast or thermally annealed at 80 and 150 °C for 15 min all show featureless morphologies, in

DOI: 10.1021/acsami.6b06365
ACS Appl. Mater. Interfaces 2016, 8, 22392–22401

which no visible aggregates or crystallites could be found (Figure 3A–C). This lack of textures in thermally annealed film of **SFBTD** is consistent with the low crystallinity of **SFBTD** we found in DSC studies. Therefore, it is not surprising that blend films containing **SFBTD**/$PC_{61}BM$ (1/4, wt/wt) do not display crystalline features (Figure 3D) even after annealing at 80 and 150 °C for 15 min (Figure 3E,F, respectively). The lack of pure donor and acceptor domains caused by poor phase separation is detrimental to charge transport, resulting in serious charge recombination as observed in the *I*–*V* curves. On the contrary, **MFBTD** thin films showed a strong tendency to crystallize. Clear and sparse needle-like crystallites can be observed in the as-cast films of **MFBTD** (Figure 3G). These crystalline features become more pronounced and form a large amount of needle-like crystals after thermal annealing at 80 °C for 15 min (Figure 3H). Surprisingly, these crystallites completely disappeared after thermally annealed at 150 °C for 15 min (Figure 3I), leading to irregularly shaped large aggregates. Even though **MFBTD** neat films show a strong tendency to crystallize, blend films of **MFBTD**/$PC_{61}BM$ (1/2, wt/wt) both as-cast and thermally annealed at 80 and 150 °C for 15 min, respectively, do not show any phase separation. This lack of phase separation and crystallization of individual components in the blend films indicates strong interactions between the donor and fullerene molecules.

The hole mobilities in neat films and BHJ blend films are measured by the space-charge limited current (SCLC) method with the hole-selective device structure: ITO/MoO_3/organic layer/MoO_3/Al (Figure S5).[45] All neat films and blend films are optimized by heating at 80 °C for 15 min before testing. Hole mobility of neat **SFBTD** film is ca. 2.0×10^{-6} cm^2 V^{-1} s^{-1}, which drastically decreases to ca. 5.9×10^{-8} cm^2 V^{-1} s^{-1} in the blend films of **SFBTD**/$PC_{61}BM$ (1/4, wt/wt). The neat **MFBTD** film displays a better hole mobility of ca. 1.7×10^{-4} cm^2 V^{-1} s^{-1}, which agrees with the observed better crystallinity of **MFBTD**. In the blend film of **MFBTD**/$PC_{61}BM$ (1/2, wt/wt), the hole mobility also decreases to ca. 6.2×10^{-6} cm^2 V^{-1} s^{-1}. Such low hole mobilities of both **SFBTD** and **MFBTD**, either as neat films or in BHJ, are expected to result in significant charge recombination and thus low J_{SC} and FF values.

The external quantum efficiency (EQE) of optimized devices employing **SFBTD** and **MFBTD** devices are shown in Figure S6. These devices show broad EQE responses from 300 to 700 nm, which matches well with the corresponding absorption profiles. The device employing **SFBTD** gives maximum EQE values between 27% and 29% from 330 to 600 nm, whereas the device employing **MFBTD** gives the maximum EQE values between 10% and 13% from 340 to 550 nm.

Since the tetrapodal structures are capable of mutual interlocking to prevent dislodging, we expect high thermal stability of OSC devices using these molecular tetrapods. Accelerated aging tests were performed on the optimized devices employing **SFBTD** and **MFBTD** by thermal annealing at 80 °C inside a N_2-filled glovebox and tested at predetermined time intervals. The aging test results are summarized in Figure S7 with device performance details given in Tables S1 and S2. After aging for 120 h, devices employing **SFBTD** lost ca. 10% of their original efficiency, while devices employing **MFBTD** lost ca. 16%. Aging test of devices employing **SFBTD** continued for a total of 384 h, after which 87% of the original efficiency was maintained. Interestingly, during the aging tests, V_{OC} values of devices employing both **SFBTD** and **MFBTD** increased initially up to 1.02 and 0.90 V, respectively, and did not change significantly with time.

Ternary Blend Devices. As we demonstrated previously, the inferior morphology and low hole mobilities of **SO**/fullerene blends could be improved by adding a low band gap and crystalline poly(3-decylthienylene vinylene) (P3DTV)[46−49] polymer (Scheme 3). The addition of P3DTV could

Scheme 3. Structures of PTV Derivatives

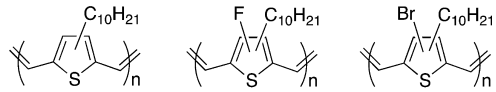

P3DTV PFDTV PBrDTV

significantly improve device efficiencies by inducing phase separation in the ternary blends.[35] Meanwhile, the addition of P3DTV, which has a higher-lying HOMO level than that of **SFBTD**, can potentially increase the hole mobility by selectively conducting holes through the more conductive conjugated polymer. Thus, **SFBTD**/P3DTV/$PC_{61}BM$ ternary blends at various weight ratios were used to fabricate the ternary solar cell devices. P3DTV (M_n = 21.3 kDa, PDI = 2.1) was synthesized according to the literature procedures[50] and used for the current study. The optimal fabrication conditions for binary P3DTV/$PC_{61}BM$ devices were found to use a 1:1 weight ratio and a thermal annealing temperature of 80 °C, yielding a PCE of ca. 0.49%. Previous literature reports have attributed the poor performance of PTV OPV devices to the extremely short exciton lifetimes.[51,52] Therefore, the weight ratios of **SFBTD**/$PC_{61}BM$ and P3DTV/$PC_{61}BM$ were kept consistent in the ternary blends at 1/4 and 1/1, respectively. Thermal annealing at 80 °C was found to slightly improve the ternary device performances. Detailed device parameters including binary and ternary blends of **SFBTD**, P3DTV, and $PCB_{61}M$ at different weight ratios are summarized in Table 2.

Compared with binary blends and ternary blends, several trends are clearly observed. The V_{OC} values of ternary devices fell steeply to the side of P3DTV as the contents of P3DTV increased. The most representative example is device B (Table 2), in which only 5 wt % of P3DTV (relative to **SFBTD**) was added, resulting in the decrease of V_{OC} from 0.88 V (device A) to 0.57 V. Unlike previous ternary examples, in which V_{OC} was found to change linearly with composition changes,[53,54] we find that the relationship in our ternary blends is far from linearity, as seen in the plots of V_{OC} vs P3DTV contents (Figure S8). This result is consistent with our recent report for **SO**/P3DTV/$PC_{61}BM$ ternary blends, which implies that, in this ternary system, the polymer serves as the major hole conductor regardless of its contents, possibly due to the high-lying HOMO level of the polymer.[35] The best performance is observed in ternary device E that displays a PCE of ca. 1.21%. Compared with the corresponding binary devices employing **SFBTD** and P3DTV alone, there is about 15% and 150% enhancement, respectively. In order to better understand the working mechanism of ternary blend and photocurrent contributions from each of the blend components, EQE experiments are performed on optimized ternary device E, as shown in Figure S9. Compared with binary device employing **SFBTD**/$PC_{61}BM$ (Figure S6A), the ternary device exhibits much more pronounced spectral responses between 600 and 750 nm, which can be ascribed from light absorption by

DOI: 10.1021/acsami.6b06365
ACS Appl. Mater. Interfaces 2016, 8, 22392−22401

Table 2. Binary and Ternary Device Performance Data Employing SFBTD and P3DTV[a]

SFBTD/P3DTV/$PC_{61}BM$[b]	V_{OC} (V)	J_{SC} (mA/cm^2)	FF (%)	PCE (%)
A. 2.5/0.0/10.0	0.88 ± 0.03 (0.92)	3.64 ± 0.17 (3.86)	33 ± 1.83 (35)	1.05 ± 0.06 (1.11)
B. 2.5/0.125/10.0	0.57 ± 0.00 (0.57)	2.50 ± 0.25 (2.87)	35 ± 0.49 (36)	0.50 ± 0.04 (0.56)
C. 2.5/1.5/11.5	0.50 ± 0.00 (0.50)	3.59 ± 0.17 (3.76)	48 ± 0.47 (48)	0.85 ± 0.04 (0.90)
D. 2.5/2.5/12.5	0.50 ± 0.01 (0.51)	3.77 ± 0.27 (4.11)	53 ± 1.50 (55)	1.01 ± 0.05 (1.09)
E. 1.5/2.5/8.5	0.49 ± 0.01 (0.50)	4.80 ± 0.33 (5.37)	52 ± 1.61 (54)	1.21 ± 0.06 (1.30)
F. 0.5/2.5/4.5	0.47 ± 0.00 (0.47)	4.33 ± 0.42 (4.96)	50 ± 0.62 (50)	1.01 ± 0.09 (1.15)
G. 0.0/2.5/2.5[c]	0.45 ± 0.00 (0.45)	2.22 ± 0.14 (2.38)	49 ± 0.84 (50)	0.49 ± 0.03 (0.53)

[a]Thermal annealing at 80 °C for 15 min. Averages of five individual cells are reported; the highest values are given in parentheses. [b]Weight ratios. [c]Thermally annealed at 80 °C for 10 min.

Table 3. Ternary Device Performance Data Employing PFDTV and PBrDTV as the Second Donor Material[a]

	V_{OC} (V)	J_{SC} (mA/cm^2)	FF (%)	PCE (%)
SFBTD/PFDTV/$PC_{61}BM$[b]				
H. 2.5/2.5/12.5	0.69 ± 0.00 (0.69)	2.20 ± 0.12 (2.37)	39 ± 1.54 (41)	0.59 ± 0.03 (0.63)
I. 1.5/2.5/8.5	0.66 ± 0.01 (0.66)	2.06 ± 0.21 (2.41)	42 ± 0.78 (43)	0.56 ± 0.06 (0.66)
J. 0.0/2.5/2.5[c]	0.66 ± 0.01 (0.68)	0.98 ± 0.05 (1.05)	49 ± 1.53 (50)	0.32 ± 0.01 (0.33)
SFBTD/PBrDTV/$PC_{61}BM$[b]				
K. 2.5/0.125/10.0	0.83 ± 0.02 (0.86)	3.37 ± 0.21 (3.78)	31 ± 0.37 (32)	0.87 ± 0.05 (0.97)
L. 2.5/2.5/12.5	0.81 ± 0.00 (0.81)	2.65 ± 0.26 (3.01)	41 ± 0.74 (42)	0.88 ± 0.09 (1.01)
M. 1.5/2.5/8.5	0.77 ± 0.01 (0.78)	2.99 ± 0.19 (3.19)	44 ± 1.96 (46)	1.01 ± 0.07 (1.14)
N. 0.0/2.5/2.5[c]	0.77 ± 0.01 (0.77)	1.91 ± 0.12 (2.12)	45 ± 1.14 (46)	0.65 ± 0.04 (0.72)

[a]Thermal annealing at 80 °C for 15 min. Averages of five individual cells are reported; the highest values are given in parentheses. [b]Weight ratios. [c]As-cast devices.

P3DTV. Despite a low V_{OC} value at ca. 0.49 V, the improvement comes from the significantly improved J_{SC} and FF values. This indicates that mixing **SFBTD** and P3DTV can produce cooperative effects on photocurrent generation by enhancing charge extraction from both of these materials. However, this cooperative effect becomes less pronounced as **SFBTD** contents increases.

It is clear that, in ternary blends with P3DTV, the low V_{OC} value, limiting the overall performance enhancement, is caused by the high-lying HOMO level of P3DTV. We thus started investigating other conjugated polymers with lower-lying HOMO levels, which may lead to higher V_{OC} values in our ternary blends with **SFBTD**. Therefore, two in-house made PTV derivatives are considered: PFDTV (M_n = 17.8 kDa, PDI = 2.0) and PBrDTV (M_n = 14.0 kDa, PDI = 2.2), as shown in Scheme 3.[55] They have similar optical band gaps, but lower HOMO levels than that of P3DTV, which are at ca. −5.2 and −5.3 eV (from CV measurement), respectively. Device parameters of ternary blends employing PFDTV and PBrDTV at various ratios are summarized in Table 3. Due to the HOMO levels of both PTV polymers that are close to that of **SFBTD**, higher V_{OC} values are achieved, which do not experience as drastic changes as that of the ternary devices employing P3DTV (Figure S8). FFs of these ternary devices are generally slightly higher than those of binary devices using **SFBTD** alone, but the overall device performances are significantly limited by low J_{SC} values. It is likely that either PFDTV or PBrDTV is not the major hole conducting material in the ternary systems due to their HOMO levels matching that of **SFBTD**, leading to unimproved charge extraction efficiencies. Thus, a judiciously experimented balance between energy level alignments, charge mobility, and phase separation is critical in ternary blend OSCs involving both small molecules and polymers, which is currently under more thorough investigations.

CONCLUSIONS

A molecular tetrapod **SFBTD** containing a tetraphenylsilance core and four fluorinated benzothiadiazole functionalized arms has been successfully prepared. UV−vis and CV measurement finds that the tetrapod has a medium band gap and a low-lying HOMO energy level. DSC studies showed that **SFBTD** has a low degree of crystallinity and slow crystallization kinetics, owing to its tetrahedral geometry. Solution-processed BHJ OPVs employing **SFBTD**/$PC_{61}BM$ without any additives and interfacial engineering exhibit a PCE of 1.05%, which is limited by the low hole mobility and unfavorable blend morphologies. The device performance of **SFBTD**/$PC_{61}BM$ binary blends could be slightly improved by adding low band gap PTV derivatives that can improve hole conduction, leading to a slight increase in device efficiencies. Our findings will benefit future studies on such molecular tetrapods and their applications in multicomponent OPVs by providing detailed structure−property relationships. Although we have shown high device stability using these molecular tetrapods, it is critical to increase the crystallization rates of these 3-D molecules and fully understand how they interact with fullerene acceptors within the blend films in order to induce proper phase separation in binary systems. On the other hand, our ternary blend studies have shown that a suitable third component with appropriate energy alignment and crystallinity can generate cooperative effects, leading to devices that out-perform those employing each of the binary components alone. We are currently investigating these aspects in more detail in order to further understand the structure−property−function relationships in this class of conjugated molecular tetrapods.

EXPERIMENTAL SECTION

Materials and General Methods. All solvents and reagents were purchased from Alfa Aesar or Sigma-Aldrich and used without further purification unless otherwise noted. 4,7-Dibromo-5-fluorobenzo[*c*]-

DOI: 10.1021/acsami.6b06365
ACS Appl. Mater. Interfaces 2016, 8, 22392−22401

[1,2,5]thiadiazole (**1**),[56] 2-(2-hexyldecyl)thiophene (**3**),[57] (5-(2-hexyldecyl)thiophen-2-yl)trimethylstannane (**4**),[57] and trimethyl(phenyl)-stannane (**11**)[58] were prepared according to literature procedures. 300.13 MHz ^{1}H, 75.48 MHz ^{13}C, and 282.37 MHz ^{19}F NMR spectra were recorded on a Bruker Avance III Solution 300 spectrometer. All solution ^{1}H and ^{13}C NMR spectra were referenced internally to solvent signals. ^{19}F NMR spectra were referenced externally to C_6F_6 (δ = −164.9 ppm). Ultraviolet−visible (UV−vis) absorption spectra were recorded on a Shimadzu UV-2401 PC spectrometer over a wavelength range of 240−900 nm. Fluorescence emission spectra were obtained using a Varian Cary Eclipse fluorimeter. Time-of-flight mass spectrometry (TOF MS) was performed on a Waters/Micromass LCT Premier system operating under atmospheric pressure photoionization ($APPI^+$) mode. Cyclic voltammetry was performed at 25 °C on a CH Instrument CHI604xD electrochemical analyzer using a glassy carbon working electrode, a platinum wire counter electrode, and a Ag/AgCl reference electrode calibrated using ferrocene redox couple (4.8 eV below vacuum). Tetrabutylammonium hexafluorophosphate (Bu_4NPF_6, 0.1 M) was used as the supporting electrolyte for the measurement. Optical Micrographs were taken on a Carl Zesis Axio Imager 2 microscope at a 400× magnification. Differential scanning calorimetry (DSC) measurements were performed on a Mettler Toledo DSC STAR^e system with ca. 10 mg sample and at scan rates of 10 and 1 °C/min. X-ray diffraction data were collected using a Rigaku SmartLab diffractometer in Bragg−Brentano mode employing Cu Kα radiation and a D/tex 1-dimensional detector. A nickel filter was used to remove the Cu Kβ radiation component. Data were collected over the 2θ range 2−40° using a 0.02° step size at a scan rate of 6.2°/min. Samples were prepared by dissolving **SFBTD** and **MFBTD** in chlorobenzene (10 mg/mL), respectively. The chlorobenzene solutions were drop-cast into glass slides and left in a fume hood to evaporate solvent until they were dry for measurement. Elemental analysis was performed by ALS Environmental Laboratory in Tucson, Arizona. Samples were analyzed by a combustion method through thermal conductivity and infrared detection.

Thin Film Preparation for UV−vis Measurements, Optical Microscopy, and Mobility Measurements. Neat films of **SFBTD** and **MFBTD** were prepared from chloroform solutions (10 mg/mL) by spin-coating onto ITO substrates. Though **SFBTD** and **MFBTD** have excellent solubility in chloroform, **MFBTD** solutions cannot wet ITO surfaces very well. Thus, neat **MFBTD** films were prepared by spin-coating at a slower spin speed of 300 rpm for 30 s, whereas neat **SFBTD** films were prepared by spin-coating at 500 rpm for 30 s. The blend films including binary and ternary blends were all prepared from chloroform solution (10 mg/mL based on **SFBTD** or **MFBTD**) by spin-coating at 500 rpm for 30 s.

Solar Cell Fabrication and Testing. A conventional structure of ITO/MoO_3 (10 nm)/active layer/Al (100 nm) was adopted for the solar cells studied. Devices were fabricated according to the following procedures. **SFBTD**, PCBM (American Dye Source, Inc.), and PTV derivatives (ternary blend) at predetermined weight ratios were dissolved in chloroform (CF) and stirred at room temperature for 3 h in a nitrogen glovebox (Innovative Technology, model PL-He-2GB, O_2 < 0.1 ppm, H_2O < 0.1 ppm). ITO-coated glass substrates (China Shenzhen Southern Glass Display. Ltd., 8 Ω/□) were cleaned by ultrasonication sequentially in detergent, DI water, acetone, and isopropyl alcohol, each for 15 min. These ITO-coated glass substrates were further treated by UV-ozone (PSD Series, Novascan) for 45 min before being transferred into a nitrogen glovebox (Innovative Technology, model PL-He-4GB-1800, O_2 < 0.1 ppm, H_2O < 0.1 ppm) for MoO_3 deposition. MoO_3 (10 nm) was deposited using an Angstrom Engineering Åmod deposition system at a base vacuum level < 7×10^{-8} Torr. The blend solution (10 mg/mL for both binary and ternary device) was first filtered through a 0.45 μm PTFE filter and spin-coated on top of the MoO_3 layer at preset speeds (1000−2000 rpm) for 30 s. Al (100 nm) was finally thermally evaporated through patterned shadow masks as anodes. Current−voltage (I−V) characteristics were measured by a Keithley 2400 source-measuring unit under simulated AM 1.5G irradiation (100 mW/cm^2) generated by a Xe arc-lamp based Newport 67005 150 W solar simulator equipped with an AM 1.5G filter. The light intensity was calibrated by using a Newport thermopile detector (model 818P-010-12) equipped with a Newport 1916-C Optical Power Meter. External quantum efficiency (EQE) values were measured by using a commercial solar cell quantum efficiency measurement system (Model QEXL, PV Measurements, Inc., Boulder, CO). The EQE system was calibrated with a Si photodiode certified by the National Renewable Energy Laboratory (NREL).

Mobility Measurement. Hole-only devices were fabricated using the architectures: ITO/MoO_3/neat film/MoO_3/Al and ITO/MoO_3/blend film/MoO_3/Al. Mobilities were extracted by fitting the current density−voltage curves using the Mott−Gurney relationship (space-charge limited current).

■ ASSOCIATED CONTENT

Supporting Information

The Supporting Information is available free of charge on the ACS Publications website at DOI: 10.1021/acsami.6b06365.

Synthesis details, time-dependent density functional theory calculation results of **MFBTD**, cyclic voltammograms of **SFBTD** and **MFBTD**, wide-angle X-ray scattering profiles of **SFBTD** and **MFBTD** thin films, current density−voltage curves of best devices, aging test data, $J^{0.5}$ vs V plots of hole mobility measurement, external quantum efficiency spectra of best devices, relation plot of V_{OC} vs P3DTV, PFDTV, and PBrDTV contents, and NMR spectra of all synthesized compounds (PDF)

■ AUTHOR INFORMATION

Corresponding Author

*E-mail: yangqin@unm.edu.

Notes

The authors declare no competing financial interest.

■ ACKNOWLEDGMENTS

The authors would like to acknowledge the University of New Mexico and the National Science Foundation (Grant Nos. IIA-1301346 and DMR-1453083) for financial support for this research.

■ REFERENCES

(1) Hoppe, H.; Sariciftci, N. S. Organic Solar Cells: An Overview. *J. Mater. Res.* **2004**, *19*, 1924−1945.

(2) Thompson, B. C.; Frechet, J. M. J. Organic Photovoltaics - Polymer-Fullerene Composite Solar Cells. *Angew. Chem., Int. Ed.* **2008**, *47*, 58−77.

(3) Dennler, G.; Scharber, M. C.; Brabec, C. J. Polymer-Fullerene Bulk-Heterojunction Solar Cells. *Adv. Mater.* **2009**, *21*, 1323−1338.

(4) Cheng, Y. J.; Yang, S. H.; Hsu, C. S. Synthesis of Conjugated Polymers for Organic Solar Cell Applications. *Chem. Rev.* **2009**, *109*, 5868−5923.

(5) Chen, H. Y.; Hou, J. H.; Zhang, S. Q.; Liang, Y. Y.; Yang, G. W.; Yang, Y.; Yu, L. P.; Wu, Y.; Li, G. Polymer Solar Cells with Enhanced Open-Circuit Voltage and Efficiency. *Nat. Photonics* **2009**, *3*, 649−653.

(6) Liang, Y. Y.; Xu, Z.; Xia, J. B.; Tsai, S. T.; Wu, Y.; Li, G.; Ray, C.; Yu, L. P. For the Bright Future-Bulk Heterojunction Polymer Solar Cells with Power Conversion Efficiency of 7.4%. *Adv. Mater.* **2010**, *22*, E135−E138.

(7) Chu, T. Y.; Lu, J. P.; Beaupre, S.; Zhang, Y. G.; Pouliot, J. R.; Wakim, S.; Zhou, J. Y.; Leclerc, M.; Li, Z.; Ding, J. F.; Tao, Y. Bulk Heterojunction Solar Cells Using Thieno[3,4-C]Pyrrole-4,6-Dione and Dithieno[3,2-B:2′,3′-D]Silole Copolymer with a Power Conversion Efficiency of 7.3%. *J. Am. Chem. Soc.* **2011**, *133*, 4250−4253.

DOI: 10.1021/acsami.6b06365
ACS Appl. Mater. Interfaces 2016, 8, 22392−22401

(8) Zhou, H. X.; Yang, L. Q.; Stuart, A. C.; Price, S. C.; Liu, S. B.; You, W. Development of Fluorinated Benzothiadiazole as a Structural Unit for a Polymer Solar Cell of 7% Efficiency. *Angew. Chem., Int. Ed.* **2011**, *50*, 2995−2998.
(9) He, Z. C.; Zhong, C. M.; Su, S. J.; Xu, M.; Wu, H. B.; Cao, Y. Enhanced Power-Conversion Efficiency in Polymer Solar Cells Using an Inverted Device Structure. *Nat. Photonics* **2012**, *6*, 591−595.
(10) Yang, T. B.; Wang, M.; Duan, C. H.; Hu, X. W.; Huang, L.; Peng, J. B.; Huang, F.; Gong, X. Inverted Polymer Solar Cells with 8.4% Efficiency by Conjugated Polyelectrolyte. *Energy Environ. Sci.* **2012**, *5*, 8208−8214.
(11) You, J.; Dou, L.; Yoshimura, K.; Kato, T.; Ohya, K.; Moriarty, T.; Emery, K.; Chen, C. C.; Gao, J.; Li, G.; Yang, Y. A Polymer Tandem Solar Cell with 10.6% Power Conversion Efficiency. *Nat. Commun.* **2013**, *4*, 1446.
(12) You, J. B.; Chen, C. C.; Hong, Z. R.; Yoshimura, K.; Ohya, K.; Xu, R.; Ye, S. L.; Gao, J.; Li, G.; Yang, Y. 10.2% Power Conversion Efficiency Polymer Tandem Solar Cells Consisting of Two Identical Sub-Cells. *Adv. Mater.* **2013**, *25*, 3973−3978.
(13) Walker, B.; Kim, C.; Nguyen, T. Q. Small Molecule Solution-Processed Bulk Heterojunction Solar Cells. *Chem. Mater.* **2011**, *23*, 470−482.
(14) Anthony, J. E. Small-Molecule, Nonfullerene Acceptors for Polymer Bulk Heterojunction Organic Photovoltaics. *Chem. Mater.* **2011**, *23*, 583−590.
(15) Szarko, J. M.; Guo, J.; Rolczynski, B. S.; Chen, L. X. Nanoscale Structure, Dynamics and Power Conversion Efficiency Correlations in Small Molecule and Oligomer-Based Photovoltaic Devices. *Nano Rev.* **2011**, *2*, 7249.
(16) Lin, Y.; Li, Y.; Zhan, X. Small Molecule Semiconductors for High-Efficiency Organic Photovoltaics. *Chem. Soc. Rev.* **2012**, *41*, 4245−4272.
(17) Mishra, A.; Bauerle, P. Small Molecule Organic Semiconductors on the Move: Promises for Future Solar Energy Technology. *Angew. Chem., Int. Ed.* **2012**, *51*, 2020−2067.
(18) Chen, Y. S.; Wan, X. J.; Long, G. K. High Performance Photovoltaic Applications Using Solution-Processed Small Molecules. *Acc. Chem. Res.* **2013**, *46*, 2645−2655.
(19) Coughlin, J. E.; Henson, Z. B.; Welch, G. C.; Bazan, G. C. Design and Synthesis of Molecular Donors for Solution-Processed High-Efficiency Organic Solar Cells. *Acc. Chem. Res.* **2014**, *47*, 257−270.
(20) Roncali, J.; Leriche, P.; Blanchard, P. Molecular Materials for Organic Photovoltaics: Small Is Beautiful. *Adv. Mater.* **2014**, *26*, 3821−3838.
(21) Jarosz, T.; Lapkowski, M.; Ledwon, P. Advances in Star-Shaped Pi-Conjugated Systems: Properties and Applications. *Macromol. Rapid Commun.* **2014**, *35*, 1006−1032.
(22) Steinmann, V.; Kronenberg, N. M.; Lenze, M. R.; Graf, S. M.; Hertel, D.; Meerholz, K.; Burckstummer, H.; Tulyakova, E. V.; Wurthner, F. Simple, Highly Efficient Vacuum-Processed Bulk Heterojunction Solar Cells Based on Merocyanine Dyes. *Adv. Energy Mater.* **2011**, *1*, 888−893.
(23) Lin, L. Y.; Chen, Y. H.; Huang, Z. Y.; Lin, H. W.; Chou, S. H.; Lin, F.; Chen, C. W.; Liu, Y. H.; Wong, K. T. A Low-Energy-Gap Organic Dye for High-Performance Small-Molecule Organic Solar Cells. *J. Am. Chem. Soc.* **2011**, *133*, 15822−15825.
(24) Fitzner, R.; Reinold, E.; Mishra, A.; Mena-Osteritz, E.; Ziehlke, H.; Korner, C.; Leo, K.; Riede, M.; Weil, M.; Tsaryova, O.; Weiss, A.; Uhrich, C.; Pfeiffer, M.; Bauerle, P. Dicyanovinyl-Substituted Oligothiophenes: Structure-Property Relationships and Application in Vacuum-Processed Small-Molecule Organic Solar Cells. *Adv. Funct. Mater.* **2011**, *21*, 897−910.
(25) Zhou, J. Y.; Wan, X. J.; Liu, Y. S.; Long, G. K.; Wang, F.; Li, Z.; Zuo, Y.; Li, C. X.; Chen, Y. S. A Planar Small Molecule with Dithienosilole Core for High Efficiency Solution-Processed Organic Photovoltaic Cells. *Chem. Mater.* **2011**, *23*, 4666−4668.
(26) Wei, G. D.; Xiao, X.; Wang, S. Y.; Zimmerman, J. D.; Sun, K.; Diev, V. V.; Thompson, M. E.; Forrest, S. R. Arylamine-Based Squaraine Donors for Use in Organic Solar Cells. *Nano Lett.* **2011**, *11*, 4261−4264.
(27) Sun, Y. M.; Welch, G. C.; Leong, W. L.; Takacs, C. J.; Bazan, G. C.; Heeger, A. J. Solution-Processed Small-Molecule Solar Cells with 6.7% Efficiency. *Nat. Mater.* **2012**, *11*, 44−48.
(28) Liu, X. F.; Sun, Y. M.; Perez, L. A.; Wen, W.; Toney, M. F.; Heeger, A. J.; Bazan, G. C. Narrow-Band-Gap Conjugated Chromophores with Extended Molecular Lengths. *J. Am. Chem. Soc.* **2012**, *134*, 20609−20612.
(29) Chen, G.; Sasabe, H.; Wang, Z. Q.; Wang, X. F.; Hong, Z. R.; Yang, Y.; Kido, J. J. Co-Evaporated Bulk Heterojunction Solar Cells with > 6.0% Efficiency. *Adv. Mater.* **2012**, *24*, 2768−2773.
(30) Talapin, D. V.; Nelson, J. H.; Shevchenko, E. V.; Aloni, S.; Sadtler, B.; Alivisatos, A. P. Seeded Growth of Highly Luminescent Cdse/Cds Nanoheterostructures with Rod and Tetrapod Morphologies. *Nano Lett.* **2007**, *7*, 2951−2959.
(31) Dayal, S.; Reese, M. O.; Ferguson, A. J.; Ginley, D. S.; Rumbles, G.; Kopidakis, N. The Effect of Nanoparticle Shape on the Photocarrier Dynamics and Photovoltaic Device Performance of Poly(3-Hexylthiophene):Cdse Nanoparticle Bulk Heterojunction Solar Cells. *Adv. Funct. Mater.* **2010**, *20*, 2629−2635.
(32) Lim, J.; Lee, D.; Park, M.; Song, J.; Lee, S.; Kang, M. S.; Lee, C.; Char, K. Modular Fabrication of Hybrid Bulk Heterojunction Solar Cells Based on Breakwater-Like Cdse Tetrapod Nanocrystal Network Infused with P3ht. *J. Phys. Chem. C* **2014**, *118*, 3942−3952.
(33) Roquet, S.; de Bettignies, R.; Leriche, P.; Cravino, A.; Roncali, J. Three-Dimensional Tetra(Oligothienyl)Silanes as Donor Material for Organic Solar Cells. *J. Mater. Chem.* **2006**, *16*, 3040−3045.
(34) Lin, Z. H.; Bjorgaard, J.; Yavuz, A. G.; Kose, M. E. Low Band Gap Star-Shaped Molecules Based on Benzothia(Oxa)Diazole for Organic Photovoltaics. *J. Phys. Chem. C* **2011**, *115*, 15097−15108.
(35) Yang, J. Z.; He, W. H.; Denman, K.; Jiang, Y. B.; Qin, Y. A Molecular Breakwater-Like Tetrapod for Organic Solar Cells. *J. Mater. Chem. A* **2015**, *3*, 2108−2119.
(36) Carsten, B.; Szarko, J. M.; Son, H. J.; Wang, W.; Lu, L. Y.; He, F.; Rolczynski, B. S.; Lou, S. J.; Chen, L. X.; Yu, L. P. Examining the Effect of the Dipole Moment on Charge Separation in Donor-Acceptor Polymers for Organic Photovoltaic Applications. *J. Am. Chem. Soc.* **2011**, *133*, 20468−20475.
(37) Rolczynski, B. S.; Szarko, J. M.; Son, H. J.; Liang, Y.; Yu, L.; Chen, L. X. Ultrafast Intramolecular Exciton Splitting Dynamics in Isolated Low-Band-Gap Polymers and Their Implications in Photovoltaic Materials Design. *J. Am. Chem. Soc.* **2012**, *134*, 4142−4152.
(38) Zang, H. D.; Liang, Y. Y.; Yu, L. P.; Hu, B. Intra-Molecular Donor-Acceptor Interaction Effects on Charge Dissociation, Charge Transport, and Charge Collection in Bulk-Heterojunction Organic Solar Cells. *Adv. Energy Mater.* **2011**, *1*, 923−929.
(39) Liu, P.; Zhang, K.; Liu, F.; Jin, Y. C.; Liu, S. J.; Russell, T. P.; Yip, H. L.; Huang, F.; Cao, Y. Effect of Fluorine Content in Thienothiophene-Benzodithiophene Copolymers on the Morphology and Performance of Polymer Solar Cells. *Chem. Mater.* **2014**, *26*, 3009−3017.
(40) Yu, G.; Gao, J.; Hummelen, J. C.; Wudl, F.; Heeger, A. J. Polymer Photovoltaic Cells - Enhanced Efficiencies Via a Network of Internal Donor-Acceptor Heterojunctions. *Science* **1995**, *270*, 1789−1791.
(41) Frisch, M. J.; Trucks, G. W.; Schlegel, H. B.; Scuseria, G. E.; Robb, M. A.; Cheeseman, J. R.; Scalmani, G.; Barone, V.; Mennucci, B.; Petersson, G. A.; Nakatsuji, H.; Caricato, M.; Li, X.; Hratchian, H. P.; Izmaylov, A. F.; Bloino, J.; Zheng, G.; Sonnenberg, J. L.; Hada, M.; Ehara, M.; Toyota, K.; Fukuda, R.; Hasegawa, J.; Ishida, M.; Nakajima, T.; Honda, Y.; Kitao, O.; Nakai, H.; Vreven, T.; Montgomery, J. A., Jr.; Peralta, J. E.; Ogliaro, F.; Bearpark, M.; Heyd, J. J.; Brothers, E.; Kudin, K. N.; Staroverov, V. N.; Kobayashi, R.; Normand, J.; Raghavachari, K.; Rendell, A.; Burant, J. C.; Iyengar, S. S.; Tomasi, J.; Cossi, M.; Rega, N.; Millam, J. M.; Klene, M.; Knox, J. E.; Cross, J. B.; Bakken, V.; Adamo, C.; Jaramillo, J.; Gomperts, R.; Stratmann, R. E.; Yazyev, O.; Austin, A. J.; Cammi, R.; Pomelli, C.; Ochterski, J. W.; Martin, R. L.; Morokuma, K.; Zakrzewski, V. G.; Voth, G. A.; Salvador, P.;

DOI: 10.1021/acsami.6b06365
ACS Appl. Mater. Interfaces 2016, 8, 22392−22401

Dannenberg, J. J.; Dapprich, S.; Daniels, A. D.; Farkas, Ö.; Foresman, J. B.; Ortiz, J. V.; Cioslowski, J.; Fox, D. J. *Gaussian 09*, Revision B.01; Gaussian, Inc.: Wallingford, CT, 2010.
(42) Dreuw, A.; Head-Gordon, M. Failure of Time-Dependent Density Functional Theory for Long-Range Charge-Transfer Excited States: The Zincbacteriochlorin-Bacterlochlorin and Bacteriochlorophyll-Spheroidene Complexes. *J. Am. Chem. Soc.* **2004**, *126*, 4007−4016.
(43) Spano, F. C. The Spectral Signatures of Frenkel Polarons in H- and J-Aggregates. *Acc. Chem. Res.* **2010**, *43*, 429−439.
(44) Lai, L. F.; Love, J. A.; Sharenko, A.; Coughlin, J. E.; Gupta, V.; Tretiak, S.; Nguyen, T. Q.; Wong, W. Y.; Bazan, G. C. Topological Considerations for the Design of Molecular Donors with Multiple Absorbing Units. *J. Am. Chem. Soc.* **2014**, *136*, 5591−5594.
(45) Malliaras, G. G.; Salem, J. R.; Brock, P. J.; Scott, C. Electrical Characteristics and Efficiency of Single-Layer Organic Light-Emitting Diodes. *Phys. Rev. B: Condens. Matter Mater. Phys.* **1998**, *58*, R13411−R13414.
(46) Zhang, C.; Matos, T.; Li, R.; Sun, S. S.; Lewis, J. E.; Zhang, J. A.; Jiang, X. M. Poly(3-Dodedyl-2,5-Thienyienevinylene)S from the Stille Coupling and the Horner-Emmons Reaction. *Polym. Chem.* **2010**, *1*, 663−669.
(47) Qin, Y.; Hillmyer, M. A. Poly(3-Hexyl-2,5-Thienylene Vinylene) by Admet Polymerization of a Dipropenyl Monomer. *Macromolecules* **2009**, *42*, 6429−6432.
(48) Kim, J. Y.; Qin, Y.; Stevens, D. A.; Ugurlu, O.; Kalihari, V.; Hillmyer, M. A.; Frisbie, C. D. Low Band Gap Poly(Thienylene Vinylene)/Fullerene Bulk Heterojunction Photovoltaic Cells. *J. Phys. Chem. C* **2009**, *113*, 10790−10797.
(49) Jestin, I.; Frere, P.; Blanchard, P.; Roncali, J. Extended Thienylenevinylene Oligomers as Highly Efficient Molecular Wires. *Angew. Chem., Int. Ed.* **1998**, *37*, 942−945.
(50) Yang, G. S.; Hu, K. D.; Qin, Y. Cis/Cis-2,5-Dipropenylthiophene Monomers for High-Molecular-Weight Poly(2,5-Thienylene Vinylene)S through Acyclic Diene Metathesis Polymerization. *J. Polym. Sci., Part A: Polym. Chem.* **2014**, *52*, 591−595.
(51) Olejnik, E.; Pandit, B.; Basel, T.; Lafalce, E.; Sheng, C. X.; Zhang, C.; Jiang, X.; Vardeny, Z. V. Ultrafast Optical Studies of Ordered Poly(3-Thienylene-Vinylene) Films. *Phys. Rev. B: Condens. Matter Mater. Phys.* **2012**, *85*, 235201.
(52) Musser, A. J.; Al-Hashimi, M.; Maiuri, M.; Brida, D.; Heeney, M.; Cerullo, G.; Friend, R. H.; Clark, J. Activated Singlet Exciton Fission in a Semiconducting Polymer. *J. Am. Chem. Soc.* **2013**, *135*, 12747−12754.
(53) Khlyabich, P. P.; Burkhart, B.; Thompson, B. C. Efficient Ternary Blend Bulk Heterojunction Solar Cells with Tunable Open-Circuit Voltage. *J. Am. Chem. Soc.* **2011**, *133*, 14534−14537.
(54) Khlyabich, P. P.; Burkhart, B.; Rudenko, A. E.; Thompson, B. C. Optimization and Simplification of Polymer-Fullerene Solar Cells through Polymer and Active Layer Design. *Polymer* **2013**, *54*, 5267−5298.
(55) Zhang, Z.; Qin, Y. Structurally Diverse Poly (Thienylene Vinylene)S (Ptvs) with Systematically Tunable Properties through Acyclic Diene Metathesis (Admet) and Postpolymerization Modification. *Macromolecules* **2016**, *49*, 3318−3327.
(56) Albrecht, S.; Janietz, S.; Schindler, W.; Frisch, J.; Kurpiers, J.; Kniepert, J.; Inal, S.; Pingel, P.; Fostiropoulos, K.; Koch, N.; Neher, D. Fluorinated Copolymer Pcpdtbt with Enhanced Open-Circuit Voltage and Reduced Recombination for Highly Efficient Polymer Solar Cells. *J. Am. Chem. Soc.* **2012**, *134*, 14932−14944.
(57) Shi, X. L.; Chang, J. J.; Chi, C. Y. Solution-Processable N-Type and Ambipolar Semiconductors Based on a Fused Cyclopentadithiophenebis(Dicyanovinylene) Core. *Chem. Commun.* **2013**, *49*, 7135−7137.
(58) Tsai, C. H.; Chirdon, D. N.; Maurer, A. B.; Bernhard, S.; Noonan, K. J. T. Synthesis of Thiophene 1,1-Dioxides and Tuning Their Optoelectronic Properties. *Org. Lett.* **2013**, *15*, 5230−5233.

DOI: 10.1021/acsami.6b06365
ACS Appl. Mater. Interfaces 2016, 8, 22392−22401